

The Role of THz Phonons in the Ionic Conduction Mechanism of $\text{Li}_7\text{La}_3\text{Zr}_2\text{O}_{12}$ Polymorphs

Amy K. Lin,[†] Natan A. Spear,[‡] Geoffrey A. Blake,[¶] and Scott K. Cushing^{*,†}

[†]*Division of Chemistry and Chemical Engineering, California Institute of Technology,
Pasadena, USA*

[‡]*Department of Applied Physics and Materials Science, California Institute of Technology,
Pasadena, USA*

[¶]*Division of Geological and Planetary Sciences, California Institute of Technology,
Pasadena, USA*

E-mail: scushing@caltech.edu

Abstract

Superionic conduction in solid-state materials is governed not only by static factors, such as structure and composition, but also by dynamic interactions between the mobile ion and the crystal lattice. Specifically, the dynamics of lattice vibrations, or phonons, have attracted interest because of their hypothesized ability to facilitate superionic conduction. However, direct experimental measurement of the role of phonons in ionic conduction is challenging due to the fast intrinsic timescales of ion hopping and the difficulty of driving relevant phonon modes, which often lie in the low-energy THz regime. To overcome these limitations, we use laser-driven ultrafast impedance spectroscopy (LUIS). LUIS resonantly excites phonons using a THz field and probes

ion hopping with picosecond time resolution. We apply LUIS to understand the dynamical role of phonons in $\text{Li}_7\text{La}_3\text{Zr}_2\text{O}_{12}$ (LLZO). When in its cubic phase (c-LLZO), this garnet-type solid electrolyte has an ionic conductivity two orders of magnitude greater than its tetragonal phase (t-LLZO). T-LLZO is characterized by an ordered and filled Li^+ sublattice necessitating synchronous ion hopping. In contrast, c-LLZO is characterized by a disordered and vacancy-rich Li^+ sublattice, and has a conduction mechanism dominated by single hops. We find that, upon excitation of phonons in the 0.5-7.5 THz range, the impedance of t-LLZO experiences a longer ion hopping decay signal in comparison to c-LLZO, which is indicative of the more frustrated ion hopping landscape. The results suggest that phonon-mediated ionic conduction by THz modes may lead to larger ion displacements in ordered and fully occupied mobile ion sublattices as opposed to those that are disordered and vacancy-rich. Overall, this work highlights the interplay between static and dynamic factors that enables improved ionic conductivity in otherwise poorly conducting inorganic solids.

Introduction

Superionic conductors are poised to replace organic liquid electrolytes in conventional Li^+ batteries, enabling safer all-solid-state energy storage technologies with increased energy density.¹⁻³ While Li^+ concentration, vacancy concentration, and structural disorder are often tuned in existing inorganic solids to enable superionic conductivity, an emerging perspective is to consider the dynamics of the crystal lattice when engineering new superionic conductors.^{4,5} Superionic conduction is inherently a dynamic process in which mobile ions interact with the surrounding framework, which is also perturbed via electrostatic and phonon interactions.⁶ Recently, there has been an influx of research focused on how specific phonon modes affect the migration of the mobile ion. For example, it has been proposed that a lower phonon band center is associated with a lower activation energy for ion hopping due to softening of the crystal lattice.⁷ Additionally, the importance of polyanion rotational phonon modes, known as the paddlewheel mechanism, is fiercely debated.^{8,9} The emphasis on phonon-ion coupling, as well as the importance of identifying low-energy phonon modes populated at room temperature, has been a growing trend in the field.¹⁰⁻¹³

To provide a complete picture of superionic conduction, one must consider the dynamic aspects of ion transport in addition to static factors, such as Li^+ occupancy. One such example is the garnet-type Li^+ conductor, $\text{Li}_7\text{La}_3\text{Zr}_2\text{O}_{12}$ (LLZO), which has garnered attention due to its low electronic conductivity, thermal and chemical stability, and wide electrochemical stability window, all of which are conditions necessary for incorporation into a solid-state battery.^{14,15} Importantly, cubic LLZO (c-LLZO) has an ionic conductivity (0.1-1 mS/cm) approaching that of liquid electrolytes (10 mS/cm).¹⁶ However, c-LLZO is only formed above $\sim 400\text{-}\sim 600$ °C, and at room temperature, its tetragonal polymorph (t-LLZO) is the stable phase.^{17,18} In both polymorphs, it is computationally postulated that Li^+ moves across LLZO's framework of ZrO_6 and LaO_8 polyhedra via junction-connected loops as illustrated in Figure 1.^{19,20} However, the ionic conductivity of t-LLZO is two orders of magnitude lower than that of c-LLZO, often attributed to differences in the Li^+ sublattices of the two poly-

morphs.^{20,21} T-LLZO has three Li sites, all fully occupied, whereas c-LLZO has two Li sites with reduced occupancy.^{19,21} The predicted occupancy values from X-ray diffraction analysis are $g = 0.94$ and $g = 0.35$ at the Li1 and Li2 sites, respectively.¹⁹ Neutron diffraction studies report an even lower occupancy of $g = 0.56$ and $g = 0.44$.²² T-LLZO has a higher activation energy (~ 0.5 eV) for ion migration because synchronous collective ion hopping is required to move through its ordered and filled Li^+ sublattice.^{20,21} Comparatively, c-LLZO with its disordered and vacancy-rich Li^+ sublattice, has a lower activation energy (~ 0.3 eV) for ion hopping, due to its crystal structure, which allows for single hops to dominate.^{20,23}

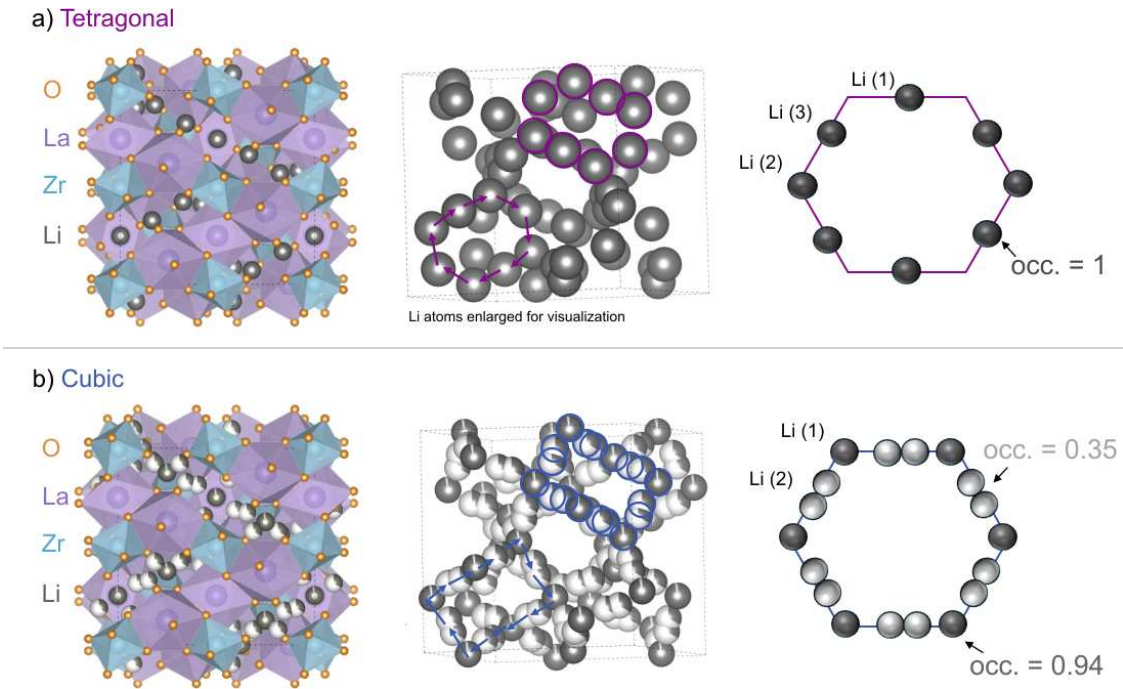


Figure 1: **Conduction pathway of (a) tetragonal and (b) cubic $\text{Li}_7\text{La}_3\text{Zr}_2\text{O}_{12}$.** Li^+ migrates across the LLZO framework of ZrO_6 and LaO_8 polyhedra, depicted in blue and purple, respectively,^{24,25} in the first column. The ions move through a 3D pathway characterized by individual loops, highlighted by the outlined Li^+ atoms, connected by junctions as shown in the second column.^{19,20} In the third column, one such hoop is shown to illustrate the order and fully occupied Li^+ sublattice of t-LLZO compared to the disordered and vacancy-rich Li^+ sublattice of c-LLZO.^{19,21}

The characterization of phonons in solid-state electrolyte candidates such as LLZO, and specifically their effects on ionic conduction, has relied on computational methods, with occasional experimental validation. In experimental studies of solid-state electrolytes, elec-

Electrochemical impedance spectroscopy (EIS) is commonly used to probe ionic conductivity across multiple timescales by applying alternating current (AC) of different frequencies.²⁶ Developments in nuclear magnetic resonance (NMR) and inelastic and quasi-elastic neutron scattering (INS and QENS, respectively) have enabled experimental characterization of ion hopping by analyzing line shifts and broadening, providing time-averaged information on structural relaxation processes and Li^+ hopping rates.^{27,28} Unfortunately, none of these methods can probe site-to-site ion hopping in real time, which is crucial for capturing the rapidly evolving dynamics of the crystal lattice, nor would any of these experimental methods, in isolation, be able to correlate the population of a set of phonons with a change in ionic conductivity.

To investigate the role of these phonons directly, on the inherent timescales of ion hopping, picoseconds time resolution and the driving of THz-range phonon modes are required. Accordingly, we use laser-driven ultrafast impedance spectroscopy (LUIS), as described in previous work, to probe changes in ion hopping in both c-LLZO and t-LLZO.^{29,30} Upon resonant excitation of THz-range phonon modes, we find a longer perturbation in the impedance of t-LLZO than c-LLZO. This indicates that phonon-mediated ionic conduction may be more effective in ordered and vacancy-rich materials as opposed to those with disordered mobile ion sublattices. Furthermore, this may indicate the presence of a THz phonon mode in LLZO that could facilitate ionic conduction. By studying many-body interactions during site-to-site hopping in real time, design rules for superionic conduction derived from phonon-ion correlations may emerge, some of which may have eluded detection through time-averaged or static lattice representation studies.

Instrumental Set-Up

Phonons of interest are in the ~ 6 THz range because the excited modes are populated at room temperature and thus are most relevant to battery operation. An ultrafast THz pulse,

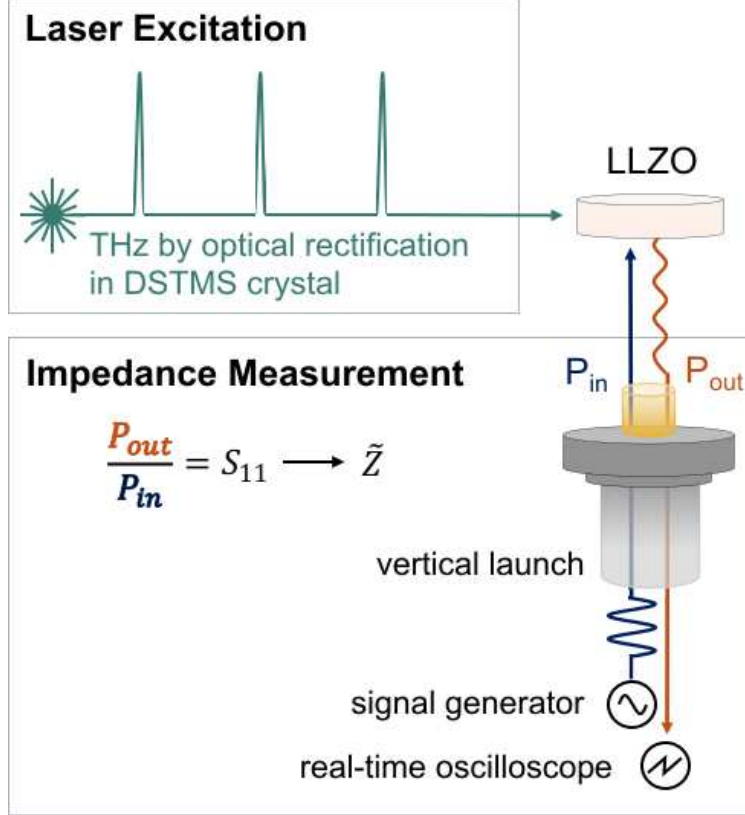


Figure 2: **Laser-driven ultrafast impedance spectroscopy (LUIS)**. Broadband 0.5-7.5 THz radiation is directed toward a $300 \mu\text{m}$ thick and 1 mm wide LLZO pellet. Orthogonally, a gigahertz (GHz) AC (blue) is transmitted to the pellet from a signal generator via a high frequency coaxial cable, a vertical launch, and finally, a gold pin which interfaces with the pellet. Impedance mismatch at that interface, in an otherwise impedance-matched system, causes a portion of the GHz signal (orange) to be reflected back through the high frequency coaxial cable and is sampled by a real-time oscilloscope. When the THz excitation causes a change in the LLZO's impedance, the perturbed GHz signal back-reflection is captured by the real-time oscilloscope.

generated by optical rectification in a DSTMS crystal with frequency content spanning 0.5-7.5 THz and a field strength of 744 kV/cm (Figure S2), resonantly excites the corresponding modes in LLZO. The LLZO pellet, $300 \mu\text{m}$ thick and 1 mm across, rests atop a gold pin connected to a high frequency coaxial cable through which an AC with a frequency and amplitude of 19 GHz and -5 dBm (172 mV sinus amplitude), respectively, is transmitted from a signal generator to the LLZO. As with EIS, the AC input frequency determines the timescale of the Li^+ migration process probed. For fast processes such as site-to-site Li hopping, GHz frequencies are required, enabling probing of processes that occur on pi-

cosecond timescales. GHz signals travel through the set up via a hybrid coupler and high frequency coaxial cables with adapters, which are impedance matched at 50Ω such that all high frequency signals are transmitted with minimal loss. At the interface of the pellet and the pin, there is an impedance mismatch, and thus some of the AC directed at the LLZO is reflected back through the transmission wire. When the THz pulse excites the phonon modes in LLZO, thereby changing its ionic conductivity, a change in impedance occurs at the LLZO-pin interface. This change thus alters the back-reflected waveform, which is captured by a real-time oscilloscope sampling every 7.8 ps. Further information on the setup, including details of the sample holder, is provided in previous work.²⁹

To isolate the perturbed signal from the noise of the GHz AC carrier wave, the oscilloscope averages the incoming waveform 1024 times. Subsequently, an amplitude demodulation function is applied, and the resulting signal is further averaged 1024 times. Finally, the root-mean-square average of the resulting spectrum is computed. Such measures are required due to the noise associated with GHz frequency circuits and the differential nature of the measurement. The goal of the measurement is not to maximally enhance ionic conduction, but instead to use THz excitations to gain a deeper insight into phonon-mediated ionic conduction. As such, the small signal must be extracted from otherwise noisy data. The final signal is fitted with an exponentially modified Gaussian function, as described in the Methods section, in which the Gaussian and exponential components capture the rise and decay of the perturbation, respectively.

Results & Discussion

Figure 3 shows a perturbation in the reflected waveform by t-LLZO and c-LLZO as a result of the THz-range excitation. It is worth noting that the c-LLZO used in this experiment is stabilized at room temperature by Nb-doping primarily at the Zr site ($\text{Li}_{6.5}\text{La}_3\text{Zr}_{1.5}\text{Nb}_{0.5}\text{O}_{12}$). X-ray diffraction of t-LLZO and c-LLZO, confirming the purity of the samples, can be found

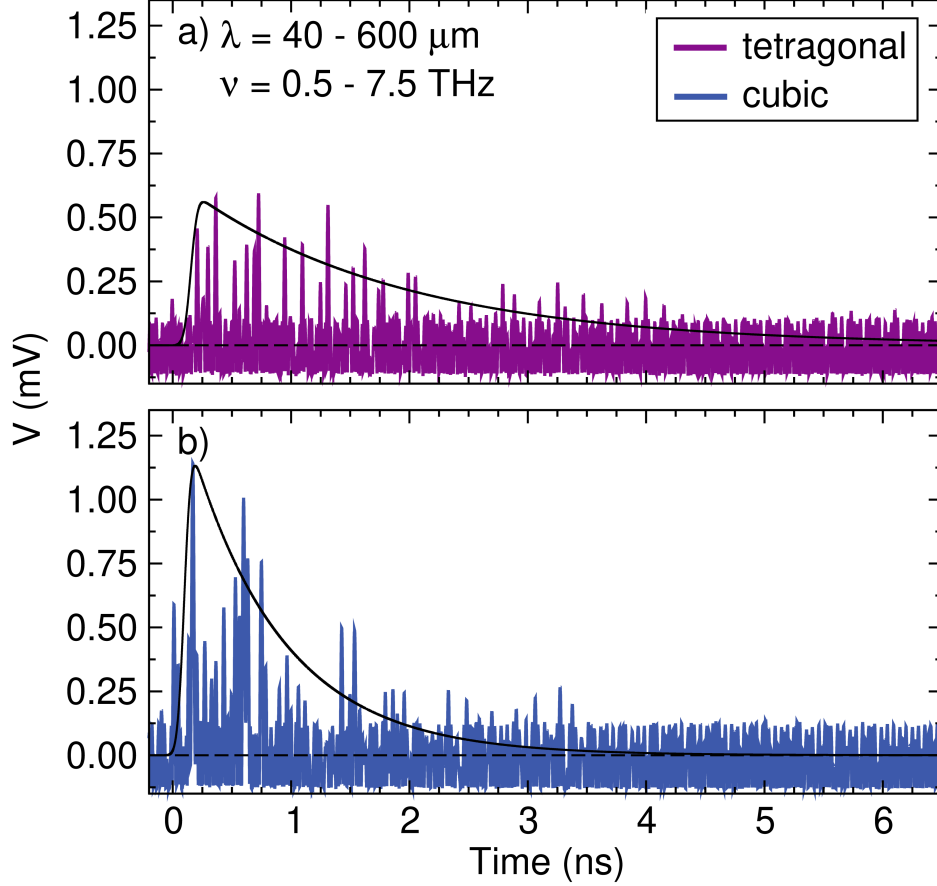


Figure 3: **THz-field-induced perturbations in (a) t-LLZO and (b) c-LLZO impedances.** The rise and decay of a perturbation in the reflected GHz signal by t-LLZO (a) and c-LLZO (b), representing their change in impedance as a result of resonantly exciting phonons between 0.5-7.5 THz by a THz field (744 kV/cm). The purple and blue signals are the root-mean-square averages of amplitude-demodulated spectra. The solid black lines are the exponentially modified Gaussian fit of each spectrum from which the decay time constant is extracted, which is ~ 900 ps and ~ 390 ps for t-LLZO and c-LLZO, respectively. The spectra have been shifted vertically so that the center of the GHz carrier is at 0, and horizontally so that time zero corresponds to the THz impulse.

in Figure S1. The decay time constant, reported here as a 95 % confidence interval, extracted from the exponentially modified Gaussian fit is 883-916 ps and 383-396 ps for t-LLZO and c-LLZO, respectively. This hundreds-of-ps decay is contrasted by the rapid decay of the perturbation when the THz pulse is replaced by a 400 nm ($\sim 12 \mu\text{J}/\text{pulse}$) or an 800 nm ($\sim 8 \mu\text{J}/\text{pulse}$) femtosecond laser excitation, as shown in Figures S3 and S4, respectively. In past experiments, sub-band gap excitation through defect states was used to to replicate

incoherent thermal heating. The decay time constants under both excitations are below 30 ps for both the t-LLZO and c-LLZO. Since the band gap of LLZO is approximately 6 eV (206 nm), 400 nm and 800 nm illumination does not excite band-edge excitations.³¹ Previous work has shown that such excitations behave similarly to laser-induced heating, such as the decay of acoustic phonons.³⁰ The difference in the length of the perturbation induced by the THz impulse relative to that induced by the 400 nm and 800 nm impulses indicates that the THz excitation drives lattice dynamics distinct laser-induced heating. Furthermore, the low electronic conductivity of LLZO, 10^{-8} S/cm, along with the large band gap of the material (6 eV) suggests that the observed change in impedance is largely caused by a change in ionic conductivity, as supported by previous UV excitation experiments.^{14,30,31}

The decay time constant of t-LLZO (~ 900 ps) is observed to be twice as long as that of c-LLZO (~ 390). We hypothesize that this difference in decay time arises from distinct Li⁺ migration processes in the two LLZO polymorphs. Li⁺ movement is synchronous in t-LLZO, so we hypothesize that the excitation of a coupled phonon-ion hopping mode will cause a larger-from-equilibrium Li⁺ displacement. Thus, in t-LLZO, the response takes longer to return to equilibrium, resulting in a relatively longer response time. In contrast, single hops dominate in vacancy-rich c-LLZO and, as such, perturbations of the crystal lattice through targeted phonon excitations have less of an effect on the equilibrium of the disordered Li⁺ sublattice. In other words, although the THz-field-driven phonon mode may facilitate the movement of these single hops throughout the crystal lattice, the abundance of unoccupied Li⁺ sites allows the material to equilibrate more quickly.

To better evaluate such a claim, the LLZO phonon baths are considered. Kim et al. compared t-LLZO with c-LLZO, using Ta to stabilize the cubic phase rather than Nb. They found that structural modes associated with La, Zr, and dopant vibrations exist in the THz regime.³² Further investigation of the phonon bath using Raman spectroscopy also reveals modes that can be indirectly excited using THz light. As seen in Figure 4, both polymorphs have relatively similar phonon baths in the low-energy THz regime. Specifically,

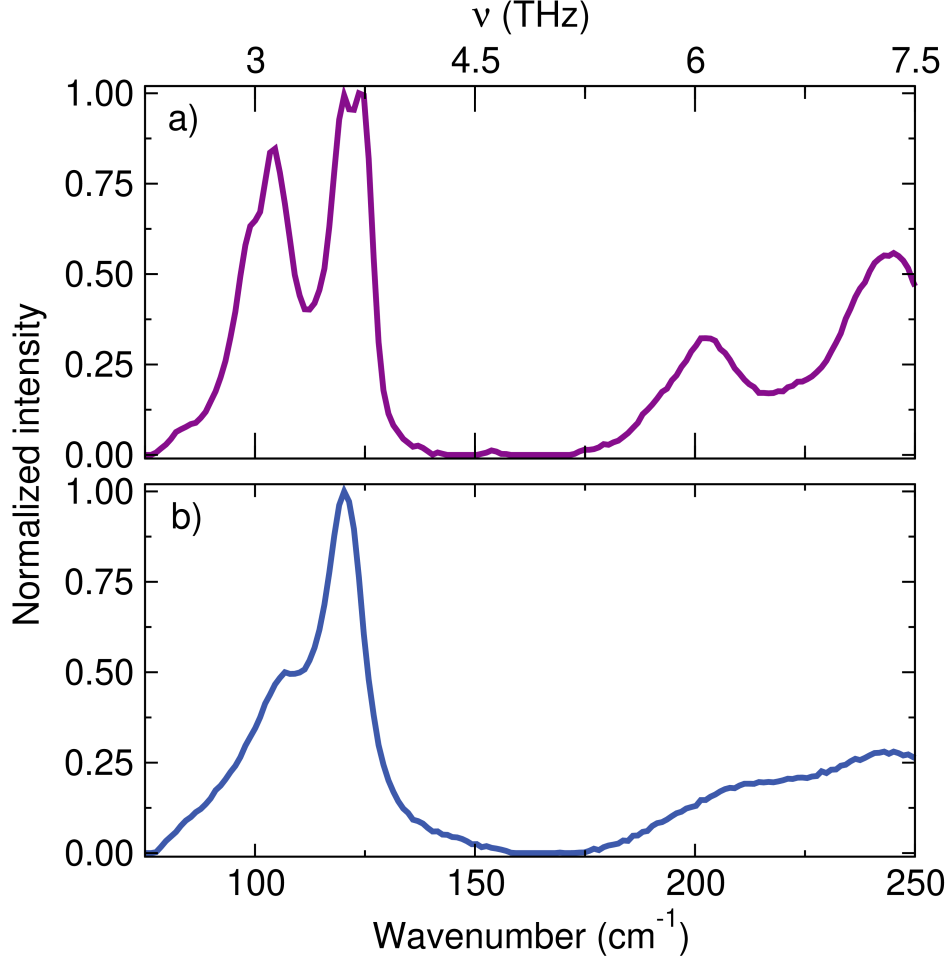


Figure 4: **Raman spectrum of (a) t-LLZO and (b) c-LLZO.** The Raman-active modes between 2.25-7.5 THz (75-250 cm^{-1}).

La-O vibrations along the Li^+ hopping pathway and diffusive Li^+ vibrations, with peak-splitting due to the differing symmetries of the two phases.³³ In the 5-7.5 THz regime, two sharp phonon peaks are observed for t-LLZO, as compared to the highly broadened modes in c-LLZO. The width of these peak indicates the degree of dynamic disorder of the phonon interactions. Given the difference in disorder of the Li sublattice between c- and t-LLZO, it is highly likely that the contrast in linewidth relates these modes to the Li ion hopping mechanism. As in, the disordered landscape in c-LLZO broadens the interacting phonon mode line-shape. In t-LLZO, the narrower linewidths reflect the more ordered sublattice and the synchronous migration mechanism. This inference is consistent with THz-active phonons playing a greater role in enhancing ionic conduction, thereby leading to a longer-

lived THz-induced LUIS response in t-LLZO. Comparatively, in vacancy-rich c-LLZO, the respective phonon modes and the disordered hopping mechanism they relate to does not cause enhanced Li^+ hopping to occur for as long as in t-LLZO.

The connection between collective migration and phonon modes is further supported by another solid state electrolyte, $\text{Li}_{3x}\text{La}_{2/3-x}\text{TiO}_3$ (LLTO). In LLTO, lattice deformation of the structural 4-O bottleneck, caused by the tilting of TiO_6 octahedra, facilitates Li^+ migration by a concerted diffusion mechanism.³⁴ In another piece of computational work, it is shown that these TiO_6 tilting modes largely reside in the regions between 1-5 THz and that ionic conductivity in LLTO is enhanced upon resonant excitation of these modes.¹³ Analogously, the 5-7.5 THz modes for t-LLZO may facilitate the synchronous movement required of t-LLZO's Li^+ sublattice for ionic conduction. We hypothesize that if inorganic solids with few vacancies can be engineered to have these types of phonon modes populated at room temperature, the high activation energies associated with the ordered mobile-ion sublattice may be overcome, and collective migration can be mediated. This type of compensation is indicative of the Meyer-Neldel Rule, which states that a decrease in activation energy does not necessarily result in an increase in ionic conductivity because it is correlated with a lower entropy of migration (prefactor) in the ionic conductivity equation.⁵ Specifically, the large entropy of migration associated with active low energy phonon modes may offset the large activation energy set by ordered mobile-ion sublattices, as indicated by the LUIS experiments in this paper. This illustrates a design strategy by which both static and dynamic factors are considered and manipulated to engineer high performing solid-state ionic conductors.

Conclusion

The tetragonal and cubic polymorphs of LLZO are a compelling pair of materials to study because, despite their similar ZrO_6 and LaO_8 framework and stoichiometry, their ionic conductivities differ by two orders of magnitude. While the pair has been investigated using

a static lattice representation, this work aims to derive design rules from dynamic-lattice measurements by examining how the population of low-energy THz phonons, which are populated at room temperature, affects their ionic conductivities. Using a THz field to resonantly excite phonons in LLZO, their impact on site-to-site Li^+ conduction is characterized by LUIS. A longer perturbation in the impedance of t-LLZO compared to c-LLZO is observed as a result of exciting the THz-range phonon modes. This suggests that phonon-mediated ionic conduction is more effective in materials like t-LLZO with a filled and ordered Li^+ sublattice compared to those whose high ionic conductivity is attributed to disorder and vacancies in its Li^+ sublattice, like c-LLZO. It can be further postulated that characteristic phonon modes, analogous to the TiO_6 tilting mode in LLTO, may be especially beneficial to facilitating ionic conduction in materials that require synchronous migration due to fewer vacancies being present. These findings offer a new investigative approach in which increasing the population of THz phonons can improve ionic conduction in otherwise poorly conducting inorganic solids.

Methods

LLZO Synthesis t-LLZO is synthesized according to literature. Stoichiometric amounts of La_2O_3 , ZrO_2 , and 10 % weight excess of Li_2CO_3 (accounts for Li loss during calcination), are mixed with a mortar and pestle. Pellets are made from the mixture using a manual Arbor press. The pellets are placed on a crucible with sacrificial powder both underneath and on its surface. The calcination is done in a furnace at 900 °C for 5 hours at a ramp rate of 1 °C/minute.

Polycrystalline Nb-doped c-LLZO is made by grounding single crystals of the material, sent from the National Institute of Advanced Industrial Science and Technology in Japan, using a mortar and pestle.

Both t-LLZO and c-LLZO are annealed according to literature. After calcination, the

t-LLZO is ground into a powder using a mortar and pestle. Both the t-LLZO and c-LLZO powders are made into 6 mm wide, 1 mm thick pellets by pressing under 2 tons of pressure for two 7 minutes with a hydraulic press. Then, the pellets are placed on a crucible and covered in sacrificial powder. The anneal step is done at 980 °C for 5 hours at a ramp rate of 1 °C/minute. Lastly, the pellets are shaved down with sandpaper to be 1 mm wide and 300 μm thick.

X-ray Diffraction of LLZO X-ray diffraction of t-LLZO and c-LLZO is obtained using a Rigaku X-ray diffractometer with $\text{CuK}\alpha$ radiation (Figure S1). The measurement is performed with a knife edge to minimize background and the LLZO powders are scanned from $2\theta = 10^\circ$ to 70° with a scan rate of $0.1^\circ/\text{minute}$. Rietveld refinement is done on the resultant spectra with GSAS II software.

Raman Spectroscopy of LLZO Raman spectra of t-LLZO and c-LLZO powders are obtained using a Horiba Instruments PLUS Raman spectrometer with a 532 nm laser. The presented spectrum is the result of 200 average spectra, each taken with an acquisition time of 1 second, at 10 % average power, with a 50 μm slit and a 500 μm hole.

Excitation Sources

800 nm: A Ti: sapphire laser is used to generate 38 femtosecond pulses of 800 nm light at a repetition rate of 1 kHz. Neutral density filters are used to bring the energy of the pulse, which excites the LLZO, to around 8 $\mu\text{J}/\text{pulse}$.

400 nm: The 800 nm light from the Ti: sapphire laser is used to pump a beta-barium borate nonlinear crystal to produce 400 nm light through second harmonic generation. Neutral density filters are used to bring the energy of the 400 nm pulse, which excites the LLZO, to around 12 $\mu\text{J}/\text{pulse}$.

THz generation: The 800 nm light from the Ti: sapphire laser is sent through an optical parametric amplifier to produce 1300 nm light with a repetition rate of 500 Hz. A DSTMS crystal is pumped by the 1300 nm light, and through optical rectification in the nonlinear crystal, a broadband THz field is generated with a field strength of 744 kV/cm and a band-

width of approximately 0.5-7.5 THz. Due to high absorption of THz frequencies by air, the THz field is maintained in a purge box back-filled with nitrogen gas.

THz detection: The THz frequency content is detected through an electro-optic sampling scheme. The P-polarized THz field passes through and thereby induces a birefringence in a GaP THz detector crystal. Linearly polarized 800 nm light from the Ti: sapphire laser hits the now birefringent GaP crystal, which changes the polarization of the 800 nm light. The arrival time of the 800 nm light is scanned such that shifts in the 800 nm polarization can be detected as a function of time by balanced photodiodes to generate a time-domain spectrum (Figure S2). Subsequently, via a fast Fourier transform of the time-domain spectrum, the frequency-domain spectrum of the generated THz field is obtained (Figure S2).

Decay Time Constant Fitting The spectra obtained through THz-excitation LUIS are fitted by the following exponentially modified Gaussian function:

$$F(t) = A \cdot e^{\left(\frac{\sigma^2}{2\tau_d^2} - \frac{t-t_0}{2\tau_d}\right)} \cdot \left[1 + \operatorname{erf}\left(\frac{t - t_0 - \frac{\sigma^2}{2\tau_d}}{\sqrt{2}\sigma}\right)\right] \quad (1)$$

where, A is the amplitude of the fit, t_0 is time zero as defined by when the sample is excited, σ is the width of the Gaussian or the instrument response time, and τ_d is the decay time constant.

Acknowledgement

The authors thank Prof. Kimberly See (Caltech) for use of her lab space for the synthesis and characterization of LLZO. The authors thank Dr. Kunimitsu Kataoka (National Institute of Advanced Industrial Science and Technology) for the c-LLZO single crystals used to synthesize the polycrystalline c-LLZO pellets used in this work. Lastly, the authors thank Jax Dallas (Caltech) for generating and characterizing the THz field used in the presented experiments.

Funding

A.K.L. acknowledges support by the the U.S. Army Research Office (ARO), grant number W911NF-23-1-0001 and the Natural Sciences and Engineering Research Council of Canada, funding reference number 599279. N.A.S. acknowledges support by the National Defense Science and Engineering Graduate Fellowship. This work was supported by the U.S. Army DEVCOM ARL Army Research Office (ARO) Energy Sciences Competency, Advanced Energy Materials Program award W911NF-23-1-0001. The equipment used in this work was funded by the Air Force Office of Scientific Research (AFOSR), DURIP grant number FA9550-23-1-0197.

The views and conclusions contained in this paper are those of the authors and should not be interpreted as representing the official policies, either expressed or implied, of the U.S. Army or the U.S. Government.

Supporting Information Available

X-ray diffraction and Raman characterization of LLZO, time and frequency domain spectra of THz field, ultrafast laser heating LUIS data.

References

- (1) Tarascon, J. M.; Armand, M. Issues and challenges facing rechargeable lithium batteries. *Nature* **2001**, *414*, 359–367.
- (2) Armand, M.; Tarascon, J. M. Building better batteries. *Nature* **2008**, *451*, 652–657.
- (3) Xu, L.; Li, J.; Deng, W.; Shuai, H.; Li, S.; Xu, Z.; Li, J.; Hou, H.; Peng, H.; Zou, G.; Ji, X. Garnet Solid Electrolyte for Advanced All-Solid-State Li Batteries. *Adv. Energy Mater.* **2020**, *11*.
- (4) Jun, K.; Chen, Y.; Wei, G.; Yang, X.; Ceder, G. Diffusion mechanisms of fast lithium-ion conductors. *Nat. Rev. Mater.* **2024**, *9*, 887–905.
- (5) Muy, S.; Schlem, R.; Shao-Horn, Y.; Zeier, W. G. Phonon–Ion Interactions: Designing Ion Mobility Based on Lattice Dynamics. *Adv. Energy Mater.* **2020**, *11*.
- (6) Song, T.; Lin, Y.; Wang, D.; Chen, Q.; Ling, C.; Shi, S. Renewing Fundamental Understanding of Ionic Transport in Inorganic Crystalline Solid-State Electrolytes from the Perspective of Lattice Dynamics. *Adv. Energy Mater.* **2024**, *14*.
- (7) Muy, S.; Bachman, J. C.; Giordano, L.; Chang, H.-H.; Abernathy, D. L.; Bansal, D.; Delaire, O.; Hori, S.; Kanno, R.; Maglia, F.; Lupart, S.; Lamph, P.; Shao-Horn, Y. Tuning mobility and stability of lithium ion conductors based on lattice dynamics. *Energy Environ. Sci.* **2018**, *11*, 850–859.
- (8) Zhang, Z.; Nazar, L. F. Exploiting the paddle-wheel mechanism for the design of fast ion conductors. *Nat. Rev. Mater.* **2022**, *7*, 389–405.
- (9) Jun, K.; Lee, B.; Kam, R. L.; Ceder, G. The nonexistence of a paddlewheel effect in superionic conductors. *Proc Natl Acad Sci U S A.* **2024**, *121*.

- (10) Ding, J.; Gupta, M. K.; Rosenbach, C.; Lin, H.-M.; Osti, N. C.; Abernathy, D. L.; Zeier, W. G.; Delaire, O. Liquid-like dynamics in a solid-state lithium electrolyte. *Nat. Phys.* **2025**, *21*, 118–125.
- (11) Gupta, M. K.; Ding, J.; Lin, H.-M.; Hood, Z.; Osti, N. C.; Abernathy, D. L.; Yakovenko, A. A.; Wang, H.; Delaire, O. Investigation of Low-Energy Lattice Dynamics and Their Role in Superionic Na Diffusion and Ultralow Thermal Conductivity of Na₃PSe₄ as a Solid-State Electrolyte. *Chem. Mater.* **2024**, *36*, 11377–11392.
- (12) Gordiz, K.; Muy, S.; Zeier, W. G.; Shao-Horn, Y.; Henry, A. Enhancement of ion diffusion by targeted phonon excitation. *Cell Rep. Phys. Sci.* **2021**, *2*.
- (13) Pham, K. H.; Gordiz, K.; Spear, N. A.; Lin, A. K.; Michelsen, J. M.; Liu, H.; Vivona, D.; Blake, G. A.; Shao-Horn, Y.; Henry, A.; See, K. A.; Cushing, S. K. Correlated Terahertz phonon-ion interactions control ion conduction in a solid electrolyte. *arXiv* **2025**,
- (14) Kravchyk, K. V.; Karabay, D. T.; Kovalenko, M. V. On the feasibility of all-solid-state batteries with LLZO as a single electrolyte. *Sci. Rep.* **2022**, *12*, 1177.
- (15) Chen, R.; Li, Q.; Yu, X.; Chen, L.; Li, H. Approaching Practically Accessible Solid-State Batteries: Stability Issues Related to Solid Electrolytes and Interfaces. *Chem. Rev.* **2020**, *120*, 6820–6877.
- (16) Murugan, R.; Thangadurai, V.; Weppner, W. Fast Lithium Ion Conduction in Garnet-Type Li₇La₃Zr₂O₁₂. *Angew. Chem. Int. Ed.* **2007**, *46*, 7778–7781.
- (17) Øystein Gullbrekken; Eggestad, K.; Tsoutsouva, M.; Williamson, B. A. D.; and Mari-Ann Einarsrud, D. R.; Selbach, S. M. Phase Evolution and Thermodynamics of Cubic Li_{6.25}Al_{0.25}La₃Zr₂O₁₂ Studied by High-Temperature X-ray Diffraction. *Angew. Chem. Int. Ed.* **2025**, *64*, 5856–5865.

- (18) Jung, S.-K.; Gwon, H.; Kim, H.; Yoon, G.; Shin, D.; Hong, J.; Jung, C.; Kim, J.-S. Unlocking the hidden chemical space in cubic-phase garnet solid electrolyte for efficient quasi-all-solid-state lithium batteries. *Nat. Commun.* **2022**, *13*, 7638.
- (19) Awaka, J.; Takashima, A.; Kataoka, K.; Kijima, N.; Idemoto, Y.; Akimoto, J. Crystal Structure of Fast Lithium-ion-conducting Cubic $\text{Li}_7\text{La}_3\text{Zr}_2\text{O}_{12}$. *Chem. Lett.* **2011**, *40*, 60–62.
- (20) Meier, K.; Laino, T.; Curioni, A. Solid-State Electrolytes: Revealing the Mechanisms of Li-Ion Conduction in Tetragonal and Cubic LLZO by First-Principles Calculations. *J. Phys. Chem. C* **2014**, *118*, 6668–6679.
- (21) Awaka, J.; Kijima, N.; Hayakawa, H.; Akimoto, J. Synthesis and structure analysis of tetragonal $\text{Li}_7\text{La}_3\text{Zr}_2\text{O}_{12}$ with the garnet-related type structure. *J. Solid State Chem.* **2009**, *182*, 2046–2052.
- (22) Xie, H.; Alonso, J. A.; Li, Y.; Fernández-Díaz, M. T.; Goodenough, J. B. Lithium Distribution in Aluminum-Free Cubic $\text{Li}_7\text{La}_3\text{Zr}_2\text{O}_{12}$. *Chem. Mater.* **2011**, *23*, 3587–3589.
- (23) Sakamoto, J.; Rangasamy, E.; Kim, H.; Kim, Y.; Wolfenstine, J. Synthesis of nano-scale fast ion conducting cubic $\text{Li}_7\text{La}_3\text{Zr}_2\text{O}_{12}$. *Nanotechnology* **2013**, *24*.
- (24) Logéat, A.; Köhler, T.; Eisele, U.; Stiaszny, B.; Harzer, A.; Tovar, M.; Senyshyn, A.; Ehrenberg, H.; Kozinsky, B. From order to disorder: The structure of lithium-conducting garnets $\text{Li}_7 - x\text{La}_3\text{TaxZr}_2 - x\text{O}_{12}$ ($x = 0-2$). *Solid State Ion.* **2012**, *206*, 33–38.
- (25) Chen, Y.; Rangasamy, E.; Liang, C.; An, K. Origin of High Li^+ Conduction in Doped $\text{Li}_7\text{La}_3\text{Zr}_2\text{O}_{12}$ Garnets. *Chem. Mater.* **2015**, *27*, 5491–5494.

- (26) Wang, S.; Zhang, J.; Gharbi, O.; Vivier, V.; Gao, M.; Orazem, M. E. Electrochemical impedance spectroscopy. *Nat. Rev. Methods Primers* **2021**, *1*.
- (27) Han, K. S.; Bazak, J. D.; Chen, Y.; Graham, T. R.; Washton, N. M.; Hu, J. Z.; Murugesan, V.; Mueller, K. T. Pulsed Field Gradient Nuclear Magnetic Resonance and Diffusion Analysis in Battery Research. *Chem. Mater.* **2021**, *3*, 8562–8590.
- (28) Schwaighofer, B.; Gonzalez, M. A.; Johnson, M. R.; Evans, J. S. O.; Evans, I. R. Ionic Mobility in Energy Materials: Through the Lens of Quasielastic Neutron Scattering. *Chem. Mater.* **2025**, *37*, 3575–3593.
- (29) Pham, K. H.; Lin, A. K.; Spear, N. A.; Cushing, S. K. Laser-driven ultrafast impedance spectroscopy for measuring complex ion hopping processes. *Rev. Sci. Instrum.* **2024**, *95*.
- (30) Pham, K. H.; Begum-Hudde, V.; Lin, A. K.; Spear, N. A.; McClellan, J.; Zuerch, M. W.; Schleife, A.; See, K. A.; Cushing, S. K. The Dynamical Role of Optical Phonons and Sublattice Screening in a Solid-State Ion Conductor. *J. Am. Chem. Soc.* **2025**, *147*, 26456–26467.
- (31) Thompson, T.; Yu, S.; Williams, L.; Schmidt, R. D.; Garcia-Mendez, R.; Wolfenshtine, J.; Allen, J. L.; Kioupakis, E.; Siegel, D. J.; Sakamoto, J. Electrochemical Window of the Li-Ion Solid Electrolyte $\text{Li}_7\text{La}_3\text{Zr}_2\text{O}_{12}$. *ACS Energy Lett.* **2017**, *2*, 462–468.
- (32) Kim, J.-B.; Kim, C.; Chung, W.; Yoon, D. H.; Lyu, L.; Jang, J.; Shin, H. J.; Nam, K.-W.; Lee, B.; Kang, Y.-M. Anharmonic Phonon Scattering Triggering Multi-ion Migration in Oxide-Based Superionic Conductors. *J. Am. Chem. Soc.* **2025**, *147*, 33743–33753.
- (33) Tietz, F.; Wegener, T.; Gerhards, M.; Giarola, M.; Mariotto, G. Synthesis and Raman micro-spectroscopy investigation of $\text{Li}_7\text{La}_3\text{Zr}_2\text{O}_{12}$. *Solid State Ion.* **2013**, *230*, 77–82.

- (34) Gao, B.; Jalem, R.; Tateyama, Y. Anharmonic Phonon Scattering Triggering Multi-ion Migration in Oxide-Based Superionic Conductors. *J. Mater. Chem. A* **2025**, *13*, 30370–30381.

SUPPLEMENTARY DOCUMENT

Enhancement of ionic conduction in $\text{Li}_7\text{La}_3\text{Zr}_2\text{O}_{12}$ polymorphs through terahertz phonon excitation

Amy K. Lin,[†] Natan A. Spear,[‡] Geoffrey A. Blake,[¶] and Scott K. Cushing^{*,†}

[†]*Division of Chemistry and Chemical Engineering, California Institute of Technology,
Pasadena, USA*

[‡]*Department of Applied Physics and Materials Science, California Institute of Technology,
Pasadena, USA*

[¶]*Division of Geological and Planetary Sciences, California Institute of Technology,
Pasadena, USA*

E-mail: scushing@caltech.edu

Supplementary Information

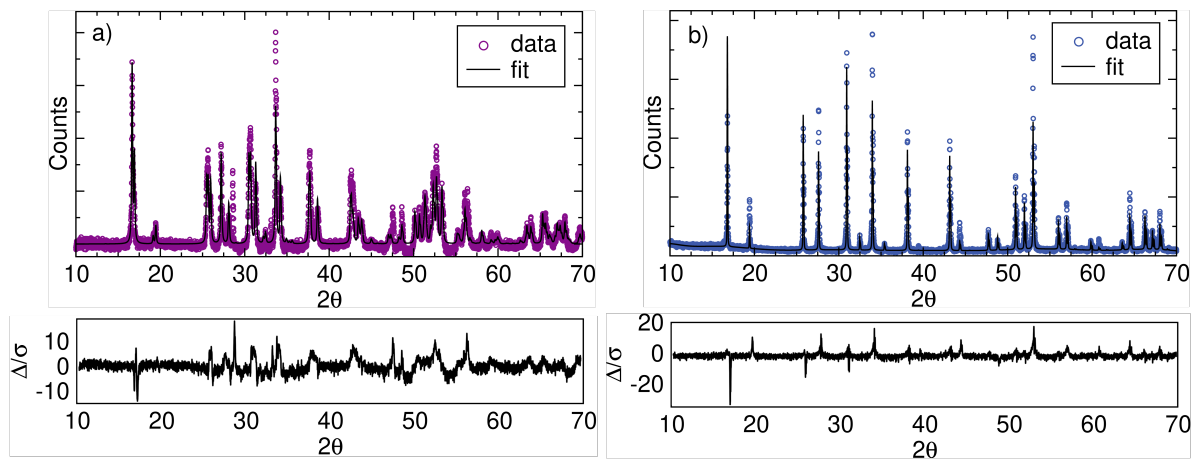


Figure S1: X-ray diffraction of (a) tetragonal and (b) cubic LLZO. a) The t-LLZO X-ray diffraction data is fitted to the space group $I 4_1/a c d$. b) The Nb-doped c-LLZO X-ray diffraction data is fitted to the space group $I a\bar{3}d$.

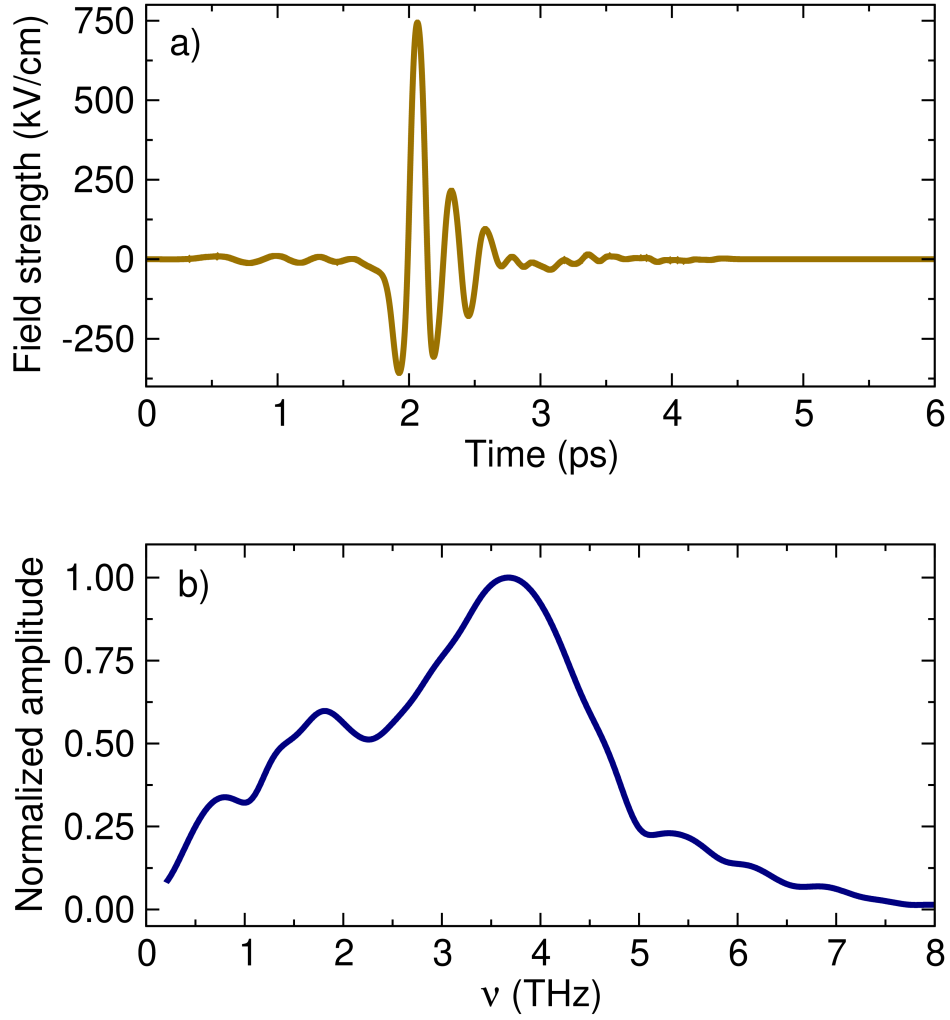


Figure S2: **Time-domain and frequency-domain spectra of THz excitation.** a) The time-domain spectrum (gold) is acquired by electro-optic detection, using a GaP crystal, of the THz field generated by optical rectification in DSTMS. b) A fast Fourier transform is used to obtain the frequency-domain spectrum (blue) of the THz field used to excite both LLZO polymorphs.

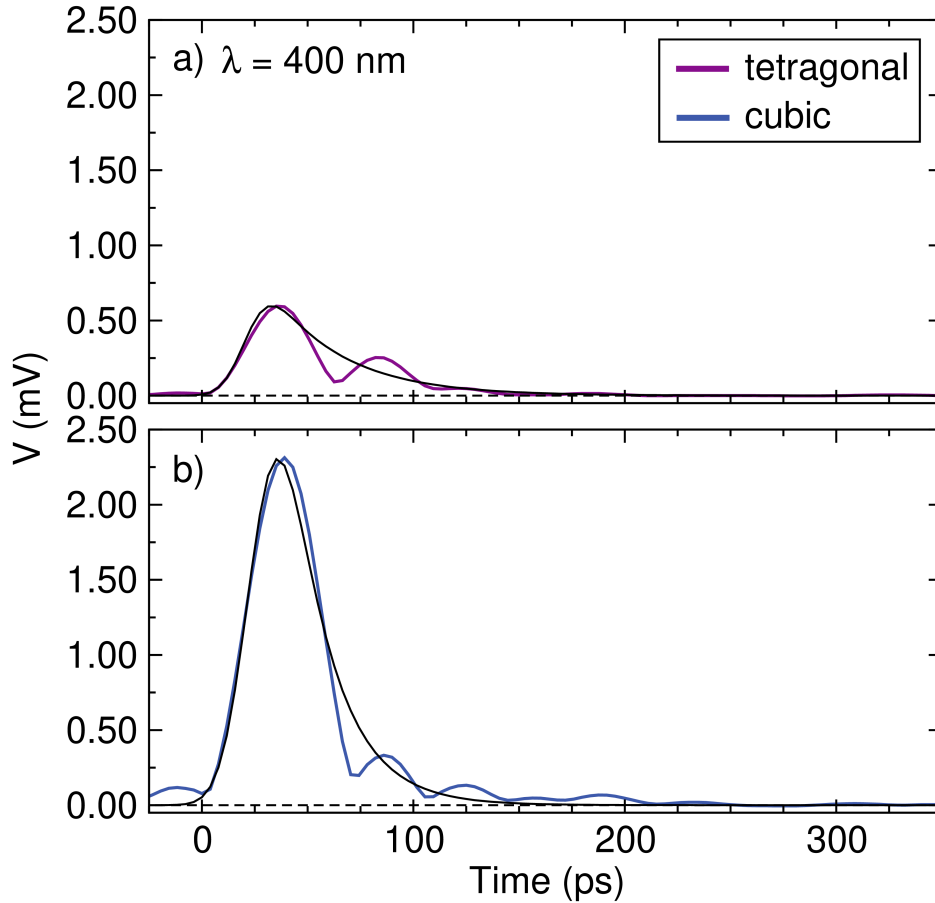


Figure S3: **400-nm-induced perturbations in (a) t-LLZO and (b) c-LLZO impedances.** The rise and decay of a perturbation in the reflected GHz waveform for (a) t-LLZO and (b) c-LLZO representing their change in impedance as a result of a 400 nm excitation ($\sim 12 \mu\text{J}/\text{pulse}$) populating defect states. The purple and blue signals are the root-mean-square averages of amplitude-demodulated spectra. The black lines are the exponentially modified Gaussian fit of each spectrum from which the decay time constant is extracted. The decay time constant, reported as a 95 % confidence interval, for t-LLZO and c-LLZO is 16.7-17.3 picoseconds and 9.83-10.2 picoseconds, respectively. The spectra have been shifted vertically such that the center of the GHz carrier frequency is at 0 and horizontally such that time zero represents the 400 nm impulse.

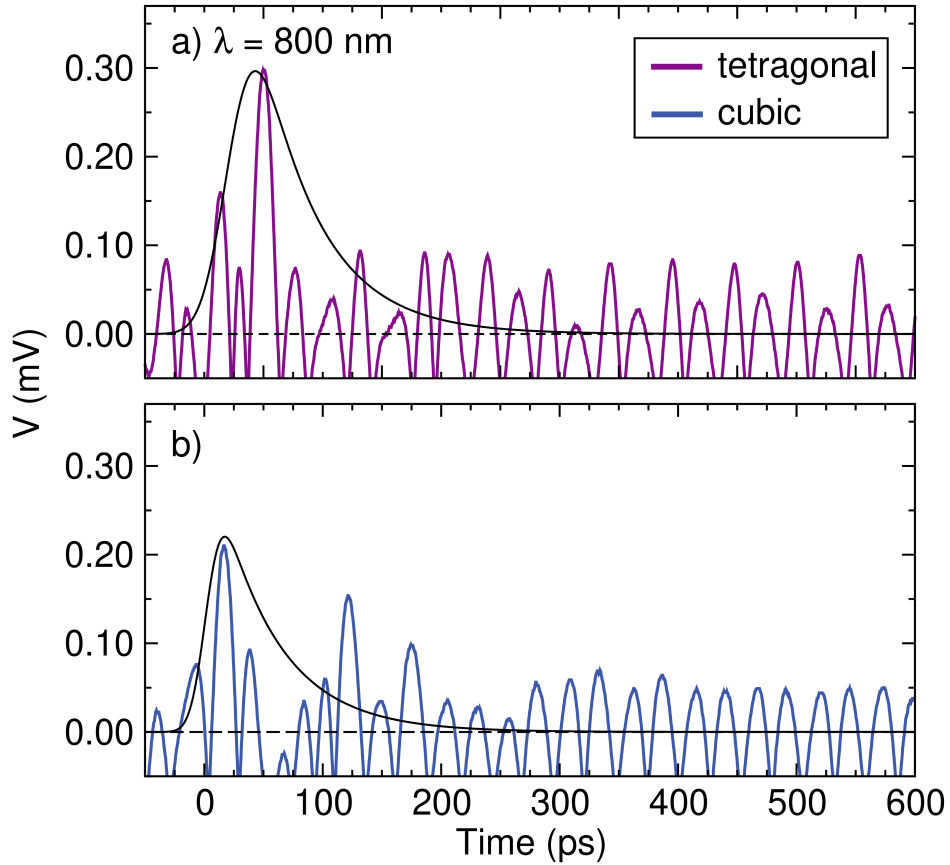


Figure S4: **800-nm-induced perturbations in (a) t-LLZO and (b) c-LLZO impedances.** The rise and decay of a perturbation in the reflected GHz waveform for (a) t-LLZO and (b) c-LLZO representing their change in impedance as a result of a 800 nm excitation ($\sim 8 \mu\text{J}/\text{pulse}$) populating defect states. The purple and blue signals are the root-mean-square averages of amplitude-demodulated spectra. The black lines are the exponentially modified Gaussian fit of each spectrum from which the decay time constant is extracted. The decay time constant, reported as a 95 % confidence interval, for t-LLZO and c-LLZO is 23.1-26.9 picoseconds and 23.0-27.0 picoseconds, respectively. The spectra have been shifted vertically such that the center of the GHz carrier frequency is at 0 and horizontally such that time zero represents the 800 nm impulse.